Revealing the Free Energy Landscape of Halide Perovskites: Metastability and Transition Characters in CsPbBr₃ and MAPbI₃

N.B. When citing this work, cite the original published paper.

(article starts on next page)

Article

Revealing the Free Energy Landscape of Halide Perovskites: Metastability and Transition Characters in CsPbBr$_3$ and MAPbI$_3$

Erik Fransson,[‡] J. Magnus Rahm,[‡] Julia Wiktor, and Paul Erhart*

Cite This: *Chem. Mater.* 2023, 35, 8229–8238

Read Online

ACCESS | Metrics & More | Article Recommendations | Supporting Information

ABSTRACT: Halide perovskites have emerged as a promising class of materials for photovoltaic applications. A challenge of these applications is preventing the crystal structure from degrading to photovoltaically inactive phases, which requires an understanding of the free energy landscape of these materials. Here, we uncover the free energy landscape of two prototypical halide perovskites, CsPbBr$_3$ and MAPbI$_3$, via atomic-scale simulations using umbrella sampling and machine-learned potentials. For CsPbBr$_3$, we find very small free energy differences and barriers close to the transition temperatures for both the tetragonal-to-cubic and orthorhombic-to-tetragonal transitions. For MAPbI$_3$, however, the situation is more intricate. In particular, the orthorhombic-to-tetragonal transition exhibits a large free energy barrier, and there

are several competing tetragonal phases. Using large-scale molecular dynamics simulations, we explore the character of these transitions and observe the latent heat and a discrete change in the structural parameters for the tetragonal-to-cubic phase transitions in both CsPbBr$_3$ and MAPbI$_3$, indicating first-order transitions. We find that in MAPbI$_3$, the orthorhombic phase has an extended metastability range, and we identify a second metastable tetragonal phase. Finally, we compile a phase diagram for MAPbI$_3$ that includes potential metastable phases.
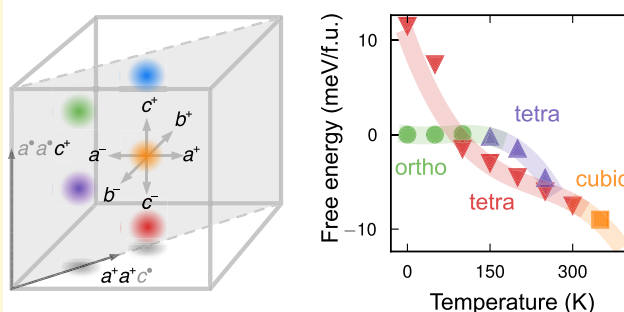
1. INTRODUCTION

Halide perovskites are highly promising materials for photovoltaic applications, with demonstrated efficiencies exceeding 25%.[1] Their application potential, however, is still limited by stability issues, which has prompted extensive research into the dynamics of their crystal structure[2–7] and the stability of different perovskite phases.[4,8–10]

In spite of the very large body of literature available, halide perovskites continue to surprise. For example, a previously not experimentally recognized crystal structure of the widely studied perovskite CsPbBr$_3$ was detected in a combination of convergent beam electron diffraction and electron ptychography.[11] Additionally, several recent studies showed that short-range ordering in octahedral tilt angles characteristic of low-temperature phases persists even in the cubic phase of halide perovskites.[6,7,12] Furthermore, the widely accepted low-temperature *Pnma* structure of MAPbI$_3$ has been put into question by a combination of inelastic neutron scattering and first-principles calculations.[13] As an alternative, the authors proposed that structures with lower local symmetry are needed to reproduce experimental data,[13] and in fact several halide perovskite structures have been shown to be locally rather similar.[14] The structural models differ, however, in properties that are crucial for photovoltaic applications, most importantly the band gap.[15] Therefore, a more detailed understanding of the local atomic structure and dynamics as well as their

coupling to phase transitions is needed for further optimization of these materials.

Similarly, the character of the phase transitions in halide perovskites has been debated. Both the tetragonal-to-cubic and orthorhombic-to-tetragonal phase transitions are driven by soft phonon modes, specifically shear modes at the M- and R-points on the Brillouin zone boundary of the cubic structure, which in the following we simply refer to as M and R modes for brevity. For a purely continuous transition, the frequency of the soft modes should go smoothly to zero at the transition temperature. However, in CsPbBr$_3$, the tetragonal-to-cubic phase transition has been observed to have first-order character through experimental studies,[16–18] whereas the transition between the tetragonal and orthorhombic phases has been characterized as purely continuous.[16] In MAPbI$_3$, the character of the tetragonal-to-cubic transition has been analyzed in numerous experimental studies with different conclusions concerning the order of the transition,[19–23] although most
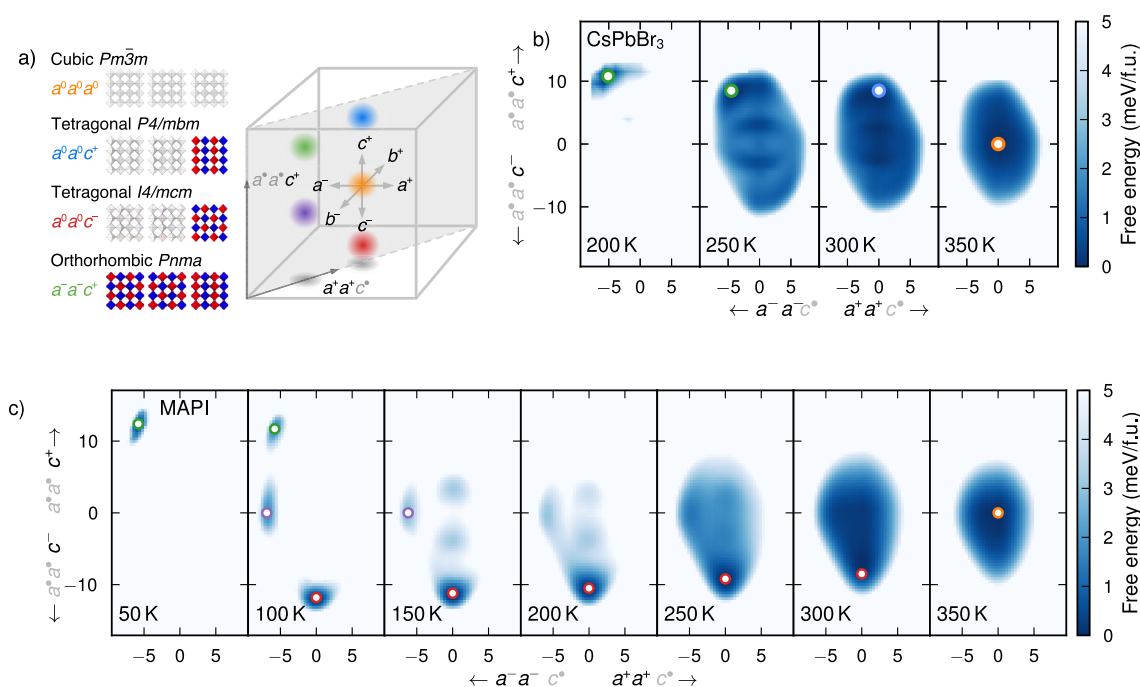
Figure 1. (a) Commonly occurring perovskite phases and their positions in Glazer space. The insets on the left-hand side show the tilting patterns along the x, y, and z directions, where red and blue indicate positive and negative tilt angles, respectively, and gray represents the absence of tilting. In addition to the four experimentally observed phases shown on the left, the figure also indicates the position of the $a^-a^-c^0$ structure (in purple), which can be observed upon heating MAPbI$_3$ if the first-order transition from $a^-a^-c^+$ to $a^0a^0c^-$ is kinetically suppressed (see Figure 2c). The atomic structures were visualized using OVITO.[63] (b and c) Free energy landscape of (b) CsPbBr$_3$ and (c) MAPbI$_3$ in Glazer space $a^\bullet b^\bullet c^\bullet$ with $a = b$. The abscissa in the free energy heat maps corresponds to the tilt angle in degrees about both the x- and y-axes, where negative and positive values indicate out-of-phase and in-phase tilting, respectively. The ordinate is the tilt angle of the z-axis.

studies point toward it being first-order. The orthorhombic-to-tetragonal transition in MAPbI$_3$ has been consistently observed to have a first-order character.

One should also note that mixing both on the cation and anion sites involving two or more different species has been demonstrated as a promising route for improving the thermodynamic stability of these materials.[24−27] This renders the configuration (and phase) space of these materials even more complex, as it adds further compositional degrees of freedom.

From a computational standpoint, the very dynamic crystal structure of halide perovskites[28,29] presents a challenge. Specifically, vibrational properties play a key role in determining the free energy landscape, and ground state density functional theory (DFT) calculations provide only very limited information in this regard. To capture the dynamic properties, ab initio molecular dynamics (MD) simulations are a popular approach, and have shone light on the band gaps of halide perovskites,[30−34] local disorder,[14,35] and defect energy levels, among other things.[36] Yet, the computational cost of ab initio MD simulations prevents extensive sampling and thereby limits access to structural and dynamic correlations that require careful convergence. Since machine-learned potentials (MLPs) have the ability to significantly speed up sampling with a negligible loss in accuracy, there has been a number of applications of these techniques to halide perovskites.[4,7,37−46] For example, Jinnouchi et al.[4] constructed an MLP for MAPbI$_3$ to study the phase transitions.[4] However, the previous studies focused on specific, predetermined phases or the transitions between them. Therefore, our understanding of the free energy landscapes of halide perovskites is still evolving.

Here, we uncover the free energy landscapes of two halide perovskites, CsPbBr$_3$ and MAPbI$_3$, with respect to the tilting degrees of freedom by constructing MLPs that are both accurate and computationally very efficient on graphics processing units (GPUs).[46,47] The structural phase space is explored via MD simulations and umbrella sampling.[48] We demonstrate that the free energy minima in CsPbBr$_3$ for the various phases are typically wide and soft with small free energy differences between phases. For MAPbI$_3$, the free energy landscape indicates a large barrier between the orthorhombic and tetragonal phases, as well as several competing tetragonal phases. We relate these results to the available tilt modes by analyzing the space of accessible tilt patterns using the concept of "Glazer space". This provides a geometrical view of the possible transitions that is transferable beyond the specific compounds and chemistries considered here. Our analysis enables us to clearly resolve the character of the different phase transitions in these systems, in agreement with the majority of experimental assignments, and eventually to construct a phase diagram for MAPbI$_3$ that includes potential metastable phases.

2. METHODS

2.1. Density Functional Theory Calculations. DFT calculations were performed using the projector augmented-wave method[49] as implemented in the Vienna ab initio simulation package.[50,51] The exchange−correlation contribution was represented using the strongly constrained and appropriately normed (SCAN) density functional,[52] which has been previously established for the study of these systems.[4,53] The Brillouin zone was sampled by using a Γ-centered grid with a k-point density of 0.25 Å^{-1} and Gaussian smearing with a width of 0.1 eV.
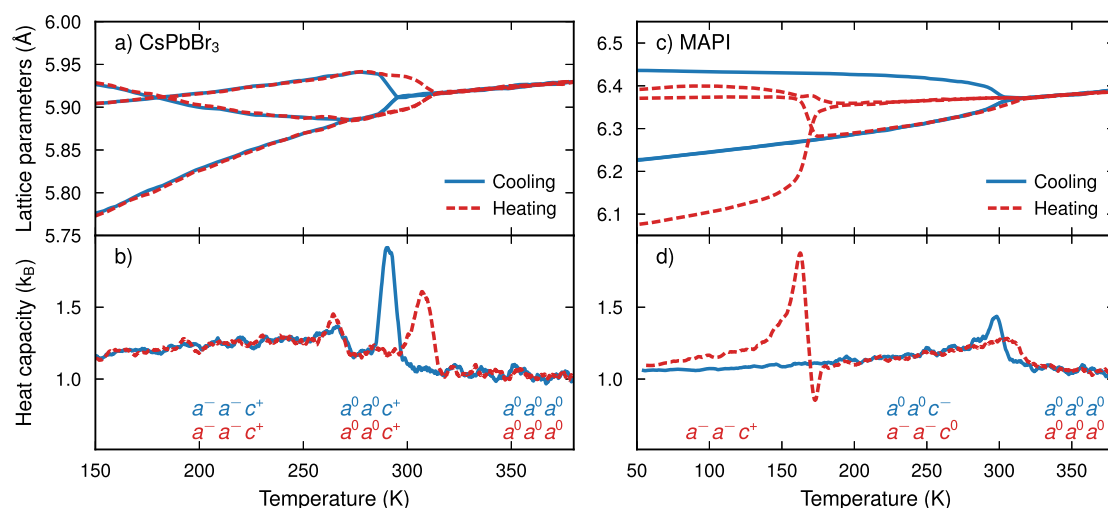
Figure 2. Lattice parameters and heat capacity from heating and cooling MD simulations in the NPT ensemble for (a and b) CsPbBr$_3$ and (c and d) MAPbI$_3$. The heat capacity is reported per degree of freedom in the system.

2.2. Neuroevolution Potentials. For CsPbBr$_3$, we employed the neuroevolution potential (NEP) model described in our recent work,[45] and for MAPbI$_3$, we constructed a model by similar means using the GPUMD package[47,48,54] in conjunction with the CALORINE[55] and ASE packages.[56] The models are based on a neural network for which the local atomic environments are described by the radial and angular components.[54] In the NEP3 version[47] employed here, the radial part of the atomic environment descriptor is constructed from linear combinations of Chebyshev basis functions, while the three-body angular part is similarly built from Legendre polynomials.

Here, we used radial and angular cutoffs of 8 and 4 Å, respectively, and terminated the radial and angular expansions at orders of 12 and 6, respectively. The neural network consisted of one hidden layer of 40 neurons with a hyperbolic tangent activation function and was trained using the natural evolution strategy[57] implemented in GPUMD, using 200 000 and 500 000 generations for training the CsPbBr$_3$ and MAPbI$_3$ models, respectively. Both the l_1 and the l_2 regularization terms were included, using $\lambda_1 = \lambda_2 = 0.02$ for CsPbBr$_3$ and $\lambda_1 = \lambda_2 = 0.05$ for MAPbI$_3$ (with λ_1 and λ_2 used as defined in ref 47). Structures for training and validation were generated by means of a bootstrapping approach, i.e., preliminary models were fitted and then new structures were extracted from MD simulations based on these models and used to fit the next model generation, similar to the approach outlined in ref 46. The final model for CsPbBr$_3$ was fitted to the forces, energies, and virials from DFT calculations of 642 atomic structures with a total of 176 920 atoms and validated against a set of 72 structures with a total of 19 800 atoms. In this holdout set, the model achieved a root-mean-square (RMS) error of 0.6 meV atom^{-1} for the energies, 15 meV atom^{-1} for the virials, and 43 meV Å^{-1} for the forces. The MAPbI$_3$ model was fitted to the forces, energies, and virials from DFT calculations of 511 atomic structures with a total of 172 092 atoms and validated against a set of 57 structures with a total of 18 804 atoms. It achieved a RMS error of 0.6 meV atom^{-1} for the energies, 4.5 meV atom^{-1} for the virials, and 38 meV Å^{-1} for the forces (see the Supporting Information for details).

2.3. Molecular Dynamics and Umbrella Sampling. MD simulations were carried out using the GPUMD package (version 3.2)[48] using a custom patch for umbrella sampling. In these simulations, time was propagated in steps of 0.5 fs in systems containing hydrogen; otherwise, a time step of 1 fs was employed. The Berendsen thermostat and barostat[58] were used to control the temperature and pressure. Systems were initialized from $4 \times 4 \times 3$ supercells of the ideal primitive orthorhombic structure for a total of 192 formula units. The system size was chosen to be large enough to avoid finite-size effects but small enough to exhibit the statistical fluctuations required for free energy integration with the weighted

histogram analysis method (WHAM) (see below). Furthermore, the global constraints in the free energy sampling become weaker for larger system sizes, and the system may not stay in the desired crystal structure but instead form interfaces or domains. The cell was constrained to remain orthorhombic, i.e., the volume was free to fluctuate, but the angles between the cell vectors were fixed to 90° throughout the simulations to simplify the analysis.

Umbrella sampling[59] was used to extract the free energy in "Glazer space" (Figure 1a and Section 3.1). To this end, we biased the simulations using six collective variables: projections ξ of atomic displacements on the three M modes and the three R modes, as done in ref 45. Each phonon mode projection was biased with a quadratic energy term

$$U_{mode} = k(\xi_{mode} - \hat{\xi}_{mode})^2$$

where ξ_{mode} is the projection on the respective phonon mode displacement (with the full displacement vector normalized to 1), $\hat{\xi}_{mode}$ is a specific target projection, and the spring constant $k = 0.1$ eV^{-1}. We performed one MD simulation of 1 ns for each combination of values of $\hat{\xi}_{mode}$ in order to span the Glazer space along the diagonal $x = y$. If the target projection of any of the modes M$_i$ was nonzero, the corresponding R$_i$ target projection was set to zero. Free energies were calculated with WHAM[60] using the software provided by Grossfield[61] but extended to handle the three-dimensional case. At low temperatures ($\leq$200 K for CsPbBr$_3$, $\leq$50 K for MAPbI$_3$) we resorted to umbrella integration, since fluctuations were too small to achieve sufficiently overlapping histograms from individual simulations.

Mapping the free energy across the Glazer space thus allows one to identify the phases corresponding to the free energy minima and their respective tilt angles and gain insight regarding the barriers between phases.[62]

3. RESULTS AND DISCUSSION

3.1. The Glazer Space. The perovskite crystal structure has the general formula ABX$_3$. The B atoms reside in corner-sharing octahedra formed by the X atoms, which in the case of halide perovskites are halide species. These octahedra tilt according to patterns that are distinctive for each phase. Typically, there are at least three phases that are stable at different temperature intervals: an orthorhombic ground state, a tetragonal phase, and a cubic phase. The tilt patterns are associated with phonon instabilities. In this regard, the three M modes and the three R modes of the cubic structure are particularly important.[45] Each M mode corresponds to the rotation of an octahedron around one of the three major axes
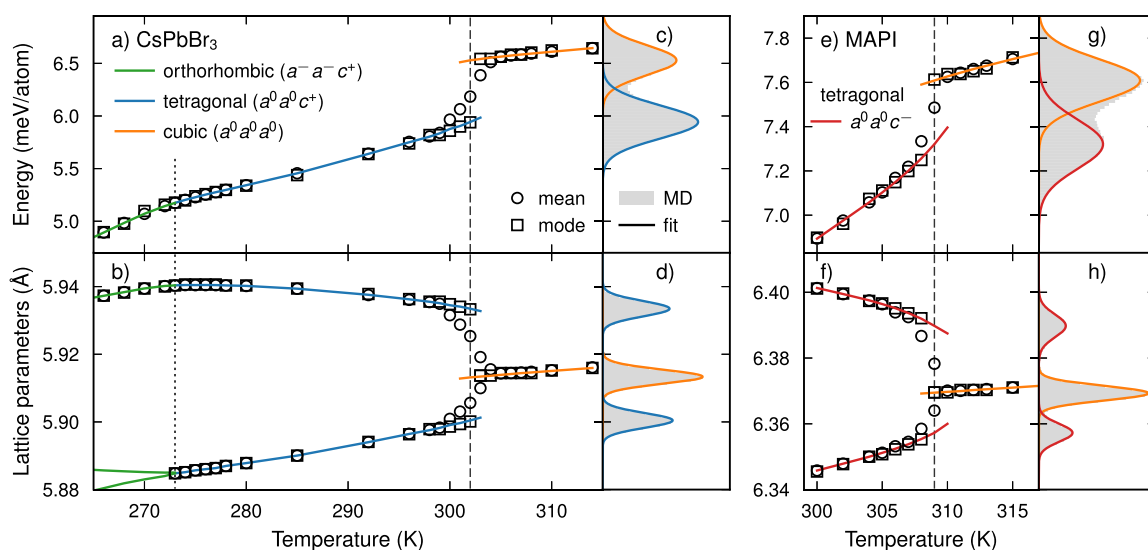
Figure 3. (a) Energy and (b) lattice parameters from MD simulations in the NPT ensemble around the cubic-to-tetragonal phase transition for CsPbBr$_3$. Here, mean denotes the average of all MD data, while mode refers to the point at which the probability is maximized. The solid lines correspond to the mean μ of the fits (Figure S3). The dotted line indicates the transition temperature between the orthorhombic and tetragonal phases. (c and d) Full distribution at 302 K, indicated by the dashed lines in (a) and (b); solid lines indicate fits (Figure S4). (e−h) The same data as in (a−d) but for MAPbI$_3$, where the histograms are shown at 309 K.

with consecutive octahedra along that axis rotated in-phase. The R modes have a similar effect, but the octahedra rotate out-of-phase. The different perovskite crystal structures are conveniently described by the projections on these modes, for which Glazer introduced a compact notation.[64] For example, the commonly occurring $Pnma$ phase can be written as $a^-a^-c^+$, which corresponds to a structure with an out-of-phase rotation of a degrees about both the x- and y-axes (the R$_x$ and R$_y$ modes) and an in-phase rotation of c degrees about the z-axis (M$_z$). The cubic phase, on the other hand, corresponds to $a^0a^0a^0$ (no average rotation about any axis). We refer to the three-dimensional space spanned by the in-phase and out-of-phase rotation about the three axes as the Glazer space (see Figure 1a for a schematic). All known stable perovskite phases of CsPbBr$_3$ and MAPbI$_3$ correspond to distinct regions in Glazer space.

3.2. CsPbBr$_3$. *Behavior on Heating/Cooling.* First, we ran heating and cooling MD simulations in the NPT ensemble for CsPbBr$_3$ with 61 440 atoms and a cooling/heating rate of about 10 K ns^{-1} (Figures 2a and 2b). Two phase transitions are observed at around 260 and 300 K, corresponding to the orthorhombic-to-tetragonal transition and the tetragonal-to-cubic transition, respectively. The transitions are clearly visible as changes in the lattice parameters, but can also be determined from peaks and kinks in the heat capacity.[46] For the tetragonal-to-cubic transition, some hysteresis is observed, suggesting first-order character, whereas for the orthorhombic-to-tetragonal transition, no hysteresis is observed, fully in line with a continuous phase transition.

Free Energy Landscape in Glazer Space. It is now instructive to consider the temperature dependence of the free energy landscape in Glazer space (Figure 1). At 350 K, the free energy minimum is found at the origin of the Glazer space, i.e., the cubic $a^0a^0a^0$ structure ($Pm\overline{3}m$). At 300 K, the free energy is lowest for the tetragonal $a^0a^0c^+$ structure ($P4/mbm$), although the free energy landscape is very flat along the z-tilt axis toward the cubic phase. The tilt angle of the tetragonal structure is about 8°. At 250 K, the free energy minimum is

found for the orthorhombic $a^-a^-c^+$ structure ($Pnma$). Finally, at 200 K, a distinct narrow free energy minimum is obtained for the $a^-a^-c^+$ phase, which continues to be the stable phase down to 0 K. The tilt angle about the z-axis is the same as in the tetragonal structure, while the tilt angle about x and y is about 4°. Again, we note that the free energy landscape between the orthorhombic $(a^-a^-c^+)$ and the tetragonal $(a^0a^0c^+)$ phase is very flat. The local free energy minimum closer to the center of the Glazer space corresponds to the $a^0a^0c^+$ phase but with multiple domains separated by antiphase boundaries, which arises due to the global constraint on the phonon mode coordinate. These can, for example, occur in a 6 × 6 × 6 (cubic) supercell with four layers of primitive cells tilting with the same phase, while the other two tilt with the opposite phase. The resulting structure has a global order parameter (mode coordinate) equal to 1/3 of the $a^0a^0c^+$ ground state.

The calculated free energy in the Glazer space contains the correct phase transitions, as observed in experiments.[16−18,65−68] They occur, however, at slightly lower temperatures, which can be attributed to the exchange− correlation functional used in the reference DFT calculations.[46]

Character of the Transitions. Next, we address the character of the transitions in CsPbBr$_3$, which are analyzed via long (20 ns), large-scale (compared to ab initio calculations; 61 440 atoms) MD simulations in the NPT ensemble in the vicinity of the transition temperature. Energy, lattice parameters, and mode projections were recorded over 10 independent simulations for each temperature. The energy referenced here is the potential energy after subtracting the zero Kelvin energy as well as the Dulong−Petit term $3k_BT/2$.

In the vicinity of the upper transition between the tetragonal and cubic phases, the histograms over the observed energy and lattice parameter values are multimodal (see Figures 3c and 3d for examples; see Figure S3 for the complete data). This behavior is due to the superposition of the distributions of the cubic and tetragonal phases, and the total histograms can be

expressed as the sum of the normal distributions (as shown in Figures 3c and 3d). We emphasize that the two phases are not observed in the MD simulations simultaneously; the system switches between the two phases over time.

As a result of the multimodal character in the vicinity of the phase transition, the mean of the distribution (circles in Figures 3a and 3b), which also corresponds to the time average of the respective quantity, changes gradually across the transition.[a]

The mode of the distribution, i.e., the position of the maximum (or most likely) value, however, exhibits a discrete jump at the transition temperature (squares in Figures 3c and 3d), which is clear evidence of the first-order character of the transition. The magnitude of the change in the potential energy yields a very small but finite latent heat of about 0.6 meV atom^{-1}. This magnitude is consistent with a first-order transition with a (very) small free energy barrier separating the phases, allowing the system to jump between the two phases on the size and time scale of our MD simulations. This barrier is also clearly visible in the mode coordinate of the M mode (Figure S2).

By contrast, for the lower (orthorhombic-to-tetragonal) transition, the distributions are unimodal, and the mean and mode coincide throughout the transition, which implies continuous character (Figure 3).

Our simulations thus show that the tetragonal-to-cubic transition is first-order while the orthorhombic-to-tetragonal transition is continuous, in agreement with experiments.[16,18] This is also consistent with our recent work on the phonon dynamics in this material, where the M mode frequency in the cubic phase was observed to be nonzero at the tetragonal-to-cubic transition temperature.[45]

3.3. MAPbI$_3$. Behavior on Heating/Cooling.

In the case of MAPbI$_3$, we observe a transition during cooling at about 300 K from the high-temperature cubic phase $(a^0a^0a^0)$ to a tetragonal structure $(a^0a^0c^-$; Figures 2c and 2d). There are no further transitions, as the system stays in the tetragonal phase down to 0 K.

On heating, starting from the orthorhombic ground state structure $(a^-a^-c^+)$, a transition occurs at around 150 K to a tetragonal (referring to $a = b \neq c$) structure[b] $(a^-a^-c^0)$ followed by another transition at 300 K to the cubic phase.

The cubic $(a^0a^0a^0)$ and orthorhombic $(a^-a^-c^+)$ phases as well as the tetragonal phase obtained on cooling $(a^0a^0c^-)$ are observed experimentally, whereas the tetragonal phase observed on heating $(a^-a^-c^0)$ is not. This is a reflection of the stochastic nature of the phase transitions. Their outcome depends on the free energy landscape at the transition temperature and is thus sensitive to both the free energy differences between possible structures and the barriers that separate them. To understand the outcome of these simulations and the nature of the phase transitions (and pathways) in MAPbI$_3$, it is instructive to inspect the free energy landscape as a function of temperature.

Free Energy Landscape in Glazer Space.

At 350 K, the free energy minimum is located at the center of the Glazer space, corresponding to the cubic phase $(a^0a^0a^0$; Figure 1c). At 300 K, the minimum has shifted to the tetragonal structure with antiphase tilting $(a^0a^0c^-)$. Similar to the case of CsPbBr$_3$ (Figure 1b), the free energy landscape close to the tetragonal-to-cubic transition is very wide and flat.

Interestingly, we also observe a local minimum in the free energy for a tetragonal $a^-a^-c^0$ structure at 100 K. Below 100 K,

the free energy minimum shifts to the orthorhombic $a^-a^-c^+$ structure. The experimental phase transition to the ortho-rhombic phase is around 160 K, which is slightly higher than the transition temperature we find here.

Character of the Tetragonal-to-Cubic Transition.

To gain further insight, we analyze the character of the tetragonal-to-cubic transition in MAPbI$_3$ in the same manner as that for CsPbBr$_3$ (Figure 3). We observe a discrete change in both the energy (latent heat) and lattice parameters, which indicates a first-order phase transition. The full distributions and corresponding fits are shown in Figure S4. The very small free energy barrier between these two phases makes the transition appear more continuous in MD simulations. This is in agreement with the near tricritical character of this transition described by Whitfield et al., who, based on experimental data, reported coexistence between the cubic and tetragonal phase in the temperature range of 300−330 K.[23] Here, we observe both phases in MD simulations in a narrow temperature interval between 305 and 310 K.

Molecular Order and Rotations.

Replacing the Cs atom with the organic MA molecule gives rise to additional degrees of freedom and renders MAPI significantly more complex than CsPbBr$_3$. Crucially, the MA units have an orientation (C−N bond vector), which is associated with ordering, in particular in the orthorhombic phase but also in the tetragonal phases.[22,53,69−73] These orientational degrees of freedom also make it much more challenging to sample the free energy landscape at low temperatures as they lead to energetic barriers between phases, which in turn allows metastable phases to remain dynamically stable down to 0 K. In order to understand the energetics of the MAPbI$_3$ phases better, we conducted an extensive sampling of possible structures (Figure 4). Ten
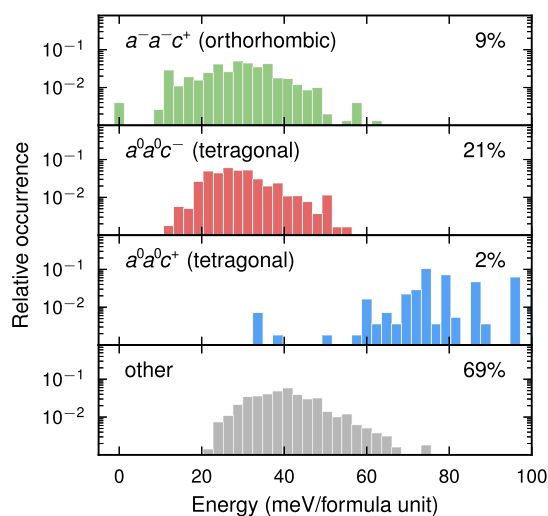

Figure 4. Energy distribution of fully relaxed MAPbI$_3$ structures obtained by generating and relaxing 10 000 possible tilted structures with randomized MA orientations in $2 \times 2 \times 2$ supercells of the primitive cubic cell.

thousand different initial structures were constructed based on $2 \times 2 \times 2$ supercells of the primitive cubic unit cell by applying a random set of tilt modes (either M or R) for each Cartesian direction with randomized amplitudes and combining that with randomized MA orientations. Each structure was relaxed (atomic positions and cell shape) until the largest force fell below 1×10^{-4} eV Å^{-1}. The relaxed structures were then

classified into the Glazer structures by projection onto the M and R modes by using a numerical tolerance of about 0.5°.

The first thing to note is that this approach correctly captures the $a^-a^-c^+$ structure as the ground state. Furthermore, it is clear that the group of tetragonal $a^0a^0c^+$ structures is significantly higher in energy compared to $a^0a^0c^-$. This is consistent with the fact that far fewer structures end up in the $a^0a^0c^-$ structure after relaxation. Yet, the majority of structures end up at slightly higher energies (>20 meV atom^{-1}), which illustrates the rather rough energy landscape of this material.

At finite temperatures, the orientations of the MA molecules fluctuate and can even flip at a significant rate, even at modest temperatures.[53,74−76] This gives rise to a sizable entropic contribution and a smoothing of the free energy landscape with increasing temperature. To analyze this aspect using the present approach, we ran MD simulations at several different temperatures starting from the lowest energy structure of each phase (Figure 4) in supercells containing 96 000 atoms. Following an equilibration for 1 ns in the NVT ensemble (at the volume obtained previously from NPT runs), the C−N bond vector $\mathbf{r}_{CN}(t)$ of each MA unit was sampled in the NVE ensemble (Figure S6). We then analyzed the rotational dynamics of MA in terms of the orientational autocorrelation function (ACF):

$$C(\tau) = \frac{\langle \mathbf{r}_{CN}^i(t)\mathbf{r}_{CN}^i(t+\tau)\rangle}{\langle \mathbf{r}_{CN}^i(t)\mathbf{r}_{CN}^i(t)\rangle} \tag{1}$$

where $\mathbf{r}_{CN}^i(t)$ is the C−N bond vector at time t for the ith MA unit. For the orthorhombic structure ($a^-a^-c^+$), one observes very few MA reorientation or rotation events on the time scales sampled here, hence they are not included in the following analysis. The ACF $C(\tau)$ exhibits oscillations on a shorter time scale (about 100 fs), corresponding to atomic vibrations, and a slow decay on a longer time scale (about 10−100 ps), corresponding to MA reorientation (Figures 5a and 5b). The latter slow rotational behavior can be modeled with one exponential decay, $C(\tau) \propto e^{-\tau/\tau_{rot}}$, where τ_{rot} corresponds to a typical rotational time (see Figure S5).[53,74] One can model the temperature dependence of the rotation time with an Arrhenius expression, $1/\tau_{rot}(T) \propto e^{-E_A/k_BT}$, which fits the data very well (Figure 5c). This yields effective activation barriers E_A for these rotational events of 120 and 103 meV for the tetragonal and cubic phases, respectively. These activation barriers are in good agreement with experimental measurements.[75,76]

Phase Diagram and Metastable Phases. Finally, we can combine the information from the heating/cooling simulations (Figures 2 and 3), the free energy landscape (Figure 1c), and the zero Kelvin energy distributions (Figure 4) to construct a free energy diagram that shows the stability ranges of the different phases observed in this work (Figure 6).

The tetragonal-to-cubic transition occurs around 309 K according to the cooling simulations. While it has first-order character, the latent heat is very small, whence it can be readily sampled in MD simulations (Figure 3). This is consistent with the free energy landscape in Glazer space, which shows the distinction between the tetragonal $a^0a^0c^-$ phase and the cubic $a^0a^0a^0$ phase to vanish slightly above 300 K (Figure 1c).

The transition from the orthorhombic $a^-a^-c^+$ to the tetragonal $a^0a^0c^-$ phase involves switching from in-phase to out-of-phase tilts relative to the c-axis and is unsurprisingly associated with a free energy barrier (Figure 1c). This prevents
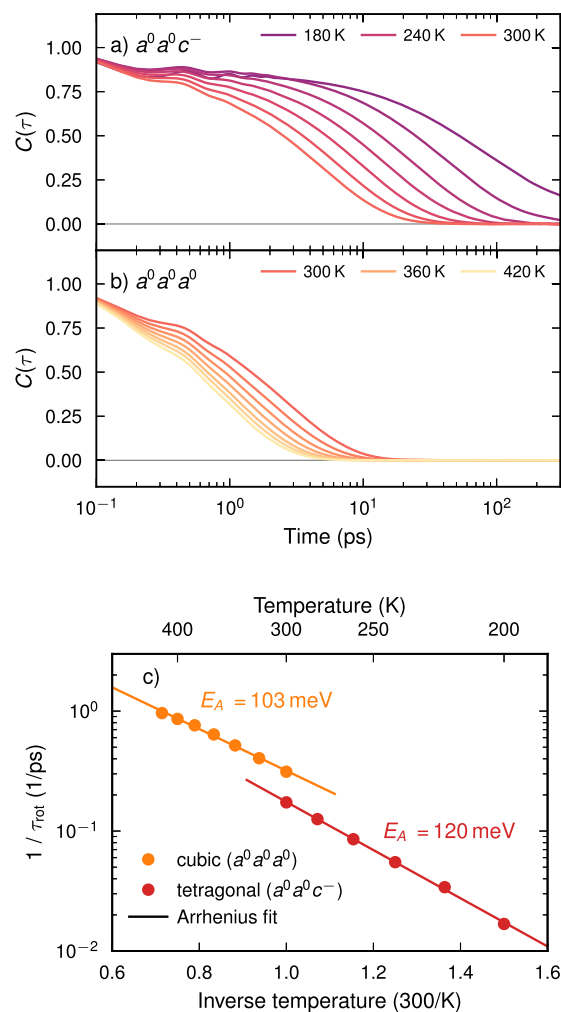

Figure 5. (a and b) Autocorrelation function $C(\tau)$ for the orientation of the MA units in each phase. The spacing between the lines is 20 K. (c) Rotation rate $1/\tau_{rot}$ obtained from (a) to (b) as a function of temperature. The solid lines correspond to Arrhenius fits $1/\tau_{rot}(T) \propto e^{-E_A/k_BT}$, where E_A is the activation barrier of the rotation process.

us from sampling this transition directly with MD simulations. Based on the free energy differences, we can, however, locate this transition at approximately 90 K. As a result of this free energy barrier, the orthorhombic $a^-a^-c^+$ remains metastable up to about 150 K (Figure 2d). Above this temperature, it becomes unstable with respect to the alternative tetragonal $a^-a^-c^0$ phase, which itself is metastable with respect to the tetragonal $a^0a^0c^-$ phase that is also observed experimentally. The metastable $a^-a^-c^0$ phase (alternatively written as $a^0b^-b^-$) is identifiable as a local free energy minimum up to about 250 K, beyond which the free energy differences become numerically too small to be resolvable.

While the present modeling does not yield the same transition temperature as experiments (caused by the approximations implicit to any current exchange−correlation functional[46]), we expect our results to be semiquantitatively correct. Hence, it is suggested that the metastability of orthorhombic $a^-a^-c^+$ is a genuine feature of MAPbI$_3$ and the result of the orientational degrees of freedom associated with the molecular MA cation. This might explain some of the uncertainty in the experimental analyses of this material.
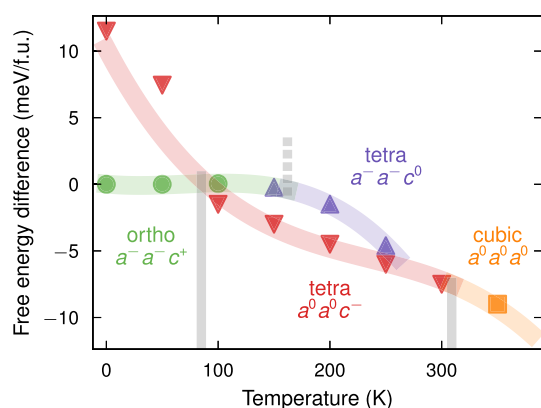
Figure 6. Phase diagram of MAPbI$_3$ constructed based on the MD simulations, free energy calculations, and energy minimization carried out in this work. Symbols represent local minima in the free energy landscape obtained from umbrella sampling (Figure 1). Lines are drawn as a guide for the eyes. Free energy differences are given relative to the orthorhombic phase at each temperature (suitably extrapolated at high temperatures). Gray horizontal lines indicate phase transition temperatures obtained from the free energy differences for the orthorhombic-to-tetragonal ($a^-a^-c^+$ to $a^0a^0c^-$) transition and from cooling MD simulations for the tetragonal-to-cubic ($a^0a^0c^-$ to $a^0a^0a^0$) transition. The dashed line indicates the transition from the orthorhombic $a^-a^-c^+$ to the tetragonal $a^-a^-c^0$ phase, as observed in the heating MD simulations (Figure 2).

Moreover, it indicates the local structural variability that can be present as well as the complexity of the underlying dynamics.

4. CONCLUSIONS

For CsPbBr$_3$, our simulations provide strong support for the cubic-to-tetragonal phase transition to have first-order character, in agreement with the majority of experimental studies. The latent heat is only on the order of a few 0.1 meV atom^{-1}, which allows one to observe the transition directly by MD simulations, even in rather large systems. We find the orthorhombic-to-tetragonal transition in CsPbBr$_3$ to be completely continuous, which overall gives rise to a rather simple free energy landscape and phase diagram.

As a result of the additional orientational degrees of freedom associated with the molecular MA cation, the situation is more complex for MAPbI$_3$. While the cubic-to-tetragonal transition has first-order character with a similarly small latent heat as in the case of CsPbBr$_3$, the low temperature of the phase diagram is notably more intricate. The orthorhombic-to-tetragonal transition has first-order character and is associated with a rather large free energy barrier that cannot be readily overcome on the length and time scales of MD simulations. In our simulations, the orthorhombic $a^-a^-c^+$ phase is found to be metastable up to about 40 K above the orthorhombic-to-tetragonal phase transition. We also identified a metastable tetragonal $a^-a^-c^0$ phase (alternatively written as $a^0b^-b^-$).

As noted before, the increased complexity of MAPbI$_3$ compared to that of CsPbBr$_3$ can be attributed to the orientational degrees of freedom associated with the molecular cation. This leads to an energy (and by extension free energy) landscape with many, usually rather shallow, local minima. Most notably, it causes the preferred tetragonal structure to switch from in-phase ($a^0a^0c^+$), which is preferred by many inorganic halide perovskites, including CsPbBr$_3$, to out-of-phase ($a^0a^0c^-$) tilting. This suggests that the trivial transition

path from the tetragonal to the orthorhombic phase involves switching from out-of-phase to in-phase tilting, suggesting an intuitive understanding of the larger free energy barrier of this transition compared to transitions in inorganic halide perovskites such as CsPbBr$_3$. The increased complexity of the (free) energy landscape moreover gives rise to metastable phases, which can in principle appear (possibly transiently) in experimental samples as well. This might explain some of the uncertainty in the experimental analyses of these materials.[13]

Orientational degrees of freedom are also present in other hybrid (organic−inorganic) perovskites, most notably FAPbI$_3$, for which one can expect similar features. It will therefore be particularly interesting to discriminate these effects in mixed systems, involving, but not limited to, MAPbI$_3$, FAPbI$_3$, and CsPbI$_3$. We hope that the present work provides a strong basis for future explorations in these directions.

■ ASSOCIATED CONTENT

Data Availability Statement

The NEP model for MAPbI$_3$ constructed in this study as well as a database with the underlying DFT calculations is openly available via Zenodo at 10.5281/zenodo.8138960. The NEP model for CsPbBr$_3$ is taken from ref 45 and is available, along with pertinent data, via Zenodo at 10.5281/zenodo.7313503.

ⓢ Supporting Information

The Supporting Information is available free of charge at https://pubs.acs.org/doi/10.1021/acs.chemmater.3c01740.

> Details pertaining to the DFT calculations (Note S1), details of the analysis of the character of the phase transitions (Note S2), figures illustrating the performance of the NEP model for MAPbI$_3$ (Figure S1), the distribution of the mode coordinate (Figure S2), the analysis of the character of the phase transitions (Figures S3 and S4), the time dependence and distribution of the orientation of MA units in MAPBI$_3$ (Figures S5 and S6), and a table comparing the energy differences from DFT calculations and the NEP model for selected MAPbI$_3$ structures (Table S1) (PDF)

■ AUTHOR INFORMATION

Corresponding Author

Paul Erhart − *Department of Physics, Chalmers University of Technology, SE-41296 Gothenburg, Sweden;* ⓘ orcid.org/0000-0002-2516-6061; Email: erhart@chalmers.se

Authors

Erik Fransson − *Department of Physics, Chalmers University of Technology, SE-41296 Gothenburg, Sweden;* ⓘ orcid.org/0000-0001-5262-3339

J. Magnus Rahm − *Department of Physics, Chalmers University of Technology, SE-41296 Gothenburg, Sweden;* ⓘ orcid.org/0000-0002-6777-0371

Julia Wiktor − *Department of Physics, Chalmers University of Technology, SE-41296 Gothenburg, Sweden;* ⓘ orcid.org/0000-0003-3395-1104

Complete contact information is available at:
https://pubs.acs.org/10.1021/acs.chemmater.3c01740

Author Contributions

‡The authors contributed equally to this work.

Notes

The authors declare no competing financial interest.

■ ACKNOWLEDGMENTS

■ ADDITIONAL NOTES

[a]We note that the width of the coexistence region in temperature as it is observed here is affected by system size as well as the strength of the barostat. It should thus not be interpreted as an experimentally accessible quantity.
[b]We refer to this phase as $a^-a^-c^0$ throughout this work to emphasize its relation to the other phases and its place in Figure [1]a. We note, however, that in the Glazer notation, it could also be written as $a^0b^-b^-$.

■ REFERENCES

(1) Best Research-Cell Efficiencies (NREL). https://www.nrel.gov/pv/cell-efficiency.html, 2023 (accessed 2023-04-15).

(2) Frost, J. M.; Walsh, A. What is moving in hybrid halide perovskite solar cells? *Acc. Chem. Res.* **2016**, *49*, 528−535.

(3) Carignano, M. A.; Aravindh, S. A.; Roqan, I. S.; Even, J.; Katan, C. Critical fluctuations and anharmonicity in lead iodide perovskites from molecular dynamics supercell simulations. *J. Phys. Chem. C* **2017**, *121*, 20729−20738.

(4) Jinnouchi, R.; Lahnsteiner, J.; Karsai, F.; Kresse, G.; Bokdam, M. Phase transitions of hybrid perovskites simulated by machine-learning force fields trained on the fly with Bayesian inference. *Phys. Rev. Lett.* **2019**, *122*, 225701.

(5) Kaiser, W.; Carignano, M.; Alothman, A. A.; Mosconi, E.; Kachmar, A.; Goddard, W. A., III; De Angelis, F. First-Principles Molecular Dynamics in Metal-Halide Perovskites: Contrasting Generalized Gradient Approximation and Hybrid Functionals. *J. Phys. Chem. Lett.* **2021**, *12*, 11886−11893.

(6) Baldwin, W.; Liang, X.; Klarbring, J.; Dubajic, M.; Dell'Angelo, D.; Sutton, C.; Caddeo, C.; Stranks, S. D.; Mattoni, A.; Walsh, A.; Csányi, G. Dynamic Local Structure in Caesium Lead Iodide: Spatial Correlation and Transient Domains. *arXiv:2304.04714* **2023**, n/a DOI: 10.48550/arXiv.2304.04714.

(7) Wiktor, J.; Fransson, E.; Kubicki, D.; Erhart, P. Quantifying Dynamic Tilting in Halide Perovskites: Chemical Trends and Local Correlations. *Chem. Mater.* **2023**, *35*, 6737−6744.

(8) Yi, C.; Luo, J.; Meloni, S.; Boziki, A.; Ashari-Astani, N.; Grätzel, C.; Zakeeruddin, S. M.; Röthlisberger, U.; Grätzel, M. Entropic stabilization of mixed A-cation ABX$_3$ metal halide perovskites for high performance perovskite solar cells. *Energy Environ. Sci.* **2016**, *9*, 656−662.

(9) Beal, R. E.; Slotcavage, D. J.; Leijtens, T.; Bowring, A. R.; Belisle, R. A.; Nguyen, W. H.; Burkhard, G. F.; Hoke, E. T.; McGehee, M. D. Cesium lead halide perovskites with improved stability for tandem solar cells. *J. Phys. Chem. Lett.* **2016**, *7*, 746−751.

(10) Raval, P.; Kennard, R. M.; Vasileiadou, E. S.; Dahlman, C. J.; Spanopoulos, I.; Chabinyc, M. L.; Kanatzidis, M.; Manjunatha Reddy, G. Understanding instability in formamidinium lead halide perovskites: Kinetics of transformative reactions at grain and subgrain boundaries. *ACS Energy Letters* **2022**, *7*, 1534−1543.

(11) dos Reis, R.; Yang, H.; Ophus, C.; Ercius, P.; Bizarri, G.; Perrodin, D.; Shalapska, T.; Bourret, E.; Ciston, J.; Dahmen, U. Determination of the structural phase and octahedral rotation angle in halide perovskites. *Appl. Phys. Lett.* **2018**, *112*, 071901.

(12) Weadock, N. J.; Sterling, T. C.; Vigil, J. A.; Gold-Parker, A.; Smith, I. C.; Ahammed, B.; Krogstad, M. J.; Ye, F.; Voneshen, D.; Gehring, P. M.; et al. The nature of dynamic local order in CH$_3$NH$_3$PbI$_3$ and CH$_3$NH$_3$PbBr$_3$. *Joule* **2023**, *7*, 1051−1066.

(13) Druzbicki, K.; Pinna, R. S.; Rudic, S.; Jura, M.; Gorini, G.; Fernandez-Alonso, F. Unexpected cation dynamics in the low-temperature phase of methylammonium lead iodide: The need for improved models. *J. Phys. Chem. Lett.* **2016**, *7*, 4701−4709.

(14) Cannelli, O.; Wiktor, J.; Colonna, N.; Leroy, L.; Puppin, M.; Bacellar, C.; Sadykov, I.; Krieg, F.; Smolentsev, G.; Kovalenko, M. V.; et al. Atomic-level description of thermal fluctuations in inorganic lead halide perovskites. *J. Phys. Chem. Lett.* **2022**, *13*, 3382−3391.

(15) Wang, T.; Daiber, B.; Frost, J. M.; Mann, S. A.; Garnett, E. C.; Walsh, A.; Ehrler, B. Indirect to direct bandgap transition in methylammonium lead halide perovskite. *Energy Environ. Sci.* **2017**, *10*, 509−515.

(16) Hirotsu, S.; Harada, J.; Iizumi, M.; Gesi, K. Structural Phase Transitions in CsPbBr$_3$. *J. Phys. Soc. Jpn.* **1974**, *37*, 1393−1398.

(17) Rodová, M.; Brožek, J.; Knížek, K.; Nitsch, K. Phase transitions in ternary caesium lead bromide. *J. Therm. Anal. Calorim.* **2003**, *71*, 667−673.

(18) Stoumpos, C. C.; Malliakas, C. D.; Peters, J. A.; Liu, Z.; Sebastian, M.; Im, J.; Chasapis, T. C.; Wibowo, A. C.; Chung, D. Y.; Freeman, A. J.; Wessels, B. W.; Kanatzidis, M. G. Crystal Growth of the Perovskite Semiconductor CsPbBr$_3$: A New Material for High-Energy Radiation Detection. *Cryst. Growth Des.* **2013**, *13*, 2722−2727.

(19) Onoda-Yamamuro, N.; Matsuo, T.; Suga, H. Calorimetric and IR spectroscopic studies of phase transitions in methylammonium trihalogenoplumbates (II). *J. Phys. Chem. Solids* **1990**, *51*, 1383−1395.

(20) Kawamura, Y.; Mashiyama, H.; Hasebe, K. Structural Study on Cubic−Tetragonal Transition of CH$_3$NH$_3$PbI$_3$. *J. Phys. Soc. Jpn.* **2002**, *71*, 1694−1697.

(21) Stoumpos, C. C.; Malliakas, C. D.; Kanatzidis, M. G. Semiconducting Tin and Lead Iodide Perovskites with Organic Cations: Phase Transitions, High Mobilities, and Near-Infrared Photoluminescent Properties. *Inorg. Chem.* **2013**, *52*, 9019−9038.

(22) Weller, M. T.; Weber, O. J.; Henry, P. F.; Di Pumpo, A. M.; Hansen, T. C. Complete structure and cation orientation in the perovskite photovoltaic methylammonium lead iodide between 100 and 352 K. *Chem. Commun.* **2015**, *51*, 4180−4183.

(23) Whitfield, P. S.; Herron, N.; Guise, W. E.; Page, K.; Cheng, Y. Q.; Milas, I.; Crawford, M. K. Structures, Phase Transitions and Tricritical Behavior of the Hybrid Perovskite Methyl Ammonium Lead Iodide. *Sci. Rep.* **2016**, *6*, 35685.

(24) McMeekin, D. P.; Sadoughi, G.; Rehman, W.; Eperon, G. E.; Saliba, M.; Hörantner, M. T.; Haghighirad, A.; Sakai, N.; Korte, L.; Rech, B.; et al. A mixed-cation lead mixed-halide perovskite absorber for tandem solar cells. *Science* **2016**, *351*, 151−155.

(25) Xu, F.; Zhang, T.; Li, G.; Zhao, Y. Mixed cation hybrid lead halide perovskites with enhanced performance and stability. *Journal of Materials Chemistry A* **2017**, *5*, 11450−11461.

(26) Kubicki, D. J.; Prochowicz, D.; Hofstetter, A.; Saski, M.; Yadav, P.; Bi, D.; Pellet, N.; Lewiński, J.; Zakeeruddin, S. M.; Grätzel, M.; Emsley, L. Formation of Stable mixed guanidinium-methylammonium phases with exceptionally long carrier lifetimes for high-efficiency lead iodide-based perovskite photovoltaics. *J. Am. Chem. Soc.* **2018**, *140*, 3345−3351.

(27) Fan, Y.; Meng, H.; Wang, L.; Pang, S. Review of stability enhancement for formamidinium-based perovskites. *Solar RRL* **2019**, *3*, 1900215.

(28) Egger, D. A.; Rappe, A. M.; Kronik, L. Hybrid organic−inorganic perovskites on the move. *Acc. Chem. Res.* **2016**, *49*, 573−581.

(29) Monacelli, L.; Marzari, N. First-Principles Thermodynamics of CsSnI$_3$. *Chem. Mater.* **2023**, *35*, 1702−1709.

(30) Carignano, M. A.; Kachmar, A.; Hutter, J. Thermal effects on $CH_3NH_3PbI_3$ perovskite from ab initio molecular dynamics simulations. *J. Phys. Chem. C* **2015**, *119*, 8991−8997.

(31) Wiktor, J.; Rothlisberger, U.; Pasquarello, A. Predictive determination of band gaps of inorganic halide perovskites. *J. Phys. Chem. Lett.* **2017**, *8*, 5507−5512.

(32) Mladenović, M.; Vukmirović, N. Effects of thermal disorder on the electronic structure of halide perovskites: Insights from MD simulations. *Phys. Chem. Chem. Phys.* **2018**, *20*, 25693−25700.

(33) Zhu, X.; Caicedo-Dávila, S.; Gehrmann, C.; Egger, D. A. Probing the Disorder Inside the Cubic Unit Cell of Halide Perovskites from First-Principles. *ACS Appl. Mater. Interfaces* **2022**, *14*, 22973−22981.

(34) Gebhardt, J.; Elsässer, C. The Electronic Structure of $Cs_2AgBiBr_6$ at Room Temperature. *physica status solidi (b)* **2022**, *259*, 2200124.

(35) Girdzis, S. P.; Lin, Y.; Leppert, L.; Slavney, A. H.; Park, S.; Chapman, K. W.; Karunadasa, H. I.; Mao, W. L. Revealing Local Disorder in a Silver-Bismuth Halide Perovskite upon Compression. *J. Phys. Chem. Lett.* **2021**, *12*, 532−536.

(36) Cohen, A. V.; Egger, D. A.; Rappe, A. M.; Kronik, L. Breakdown of the static picture of defect energetics in halide perovskites: the case of the Br vacancy in $CsPbBr_3$. *J. Phys. Chem. Lett.* **2019**, *10*, 4490−4498.

(37) Lahnsteiner, J.; Jinnouchi, R.; Bokdam, M. Long-range order imposed by short-range interactions in methylammonium lead iodide: comparing point-dipole models to machine-learning force fields. *Phys. Rev. B* **2019**, *100*, 094106.

(38) Thomas, J. C.; Bechtel, J. S.; Natarajan, A. R.; Van der Ven, A. Machine learning the density functional theory potential energy surface for the inorganic halide perovskite $CsPbBr_3$. *Phys. Rev. B* **2019**, *100*, 134101.

(39) Zhou, G.; Chu, W.; Prezhdo, O. V. Structural deformation controls charge losses in $MAPbI_3$: Unsupervised machine learning of nonadiabatic molecular dynamics. *ACS Energy Letters* **2020**, *5*, 1930.

(40) Mangan, S. M.; Zhou, G.; Chu, W.; Prezhdo, O. V. Dependence between Structural and Electronic Properties of $CsPbI_3$: Unsupervised Machine Learning of Nonadiabatic Molecular Dynamics. *J. Phys. Chem. Lett.* **2021**, *12*, 8672−8678.

(41) Bokdam, M.; Lahnsteiner, J.; Sarma, D. Exploring Librational Pathways with on-the-Fly Machine-Learning Force Fields: Methyl-ammonium Molecules in $MAPbX_3$ (X = I, Br, Cl) Perovskites. *J. Phys. Chem. C* **2021**, *125*, 21077−21086.

(42) Gruninger, H.; Bokdam, M.; Leupold, N.; Tinnemans, P.; Moos, R.; De Wijs, G. A.; Panzer, F.; Kentgens, A. P. M. Microscopic (dis)order and dynamics of cations in mixed FA/MA lead halide perovskites. *J. Phys. Chem. C* **2021**, *125*, 1742−1753.

(43) Lahnsteiner, J.; Bokdam, M. Anharmonic lattice dynamics in large thermodynamic ensembles with machine-learning force fields: $CsPbBr_3$, a phonon liquid with Cs rattlers. *Phys. Rev. B* **2022**, *105*, 024302.

(44) Braeckevelt, T.; Goeminne, R.; Vandenhaute, S.; Borgmans, S.; Verstraelen, T.; Steele, J. A.; Roeffaers, M. B. J.; Hofkens, J.; Rogge, S. M. J.; Van Speybroeck, V. Accurately Determining the Phase Transition Temperature of $CsPbI_3$ via Random-Phase Approximation Calculations and Phase-Transferable Machine Learning Potentials. *Chem. Mater.* **2022**, *34*, 8561−8576.

(45) Fransson, E.; Rosander, P.; Eriksson, F.; Rahm, J. M.; Tadano, T.; Erhart, P. Limits of the phonon quasi-particle picture at the cubic-to-tetragonal phase transition in halide perovskites. *Communications Physics* **2023**, *6*, 173.

(46) Fransson, E.; Wiktor, J.; Erhart, P. Phase transitions in inorganic halide perovskites from machine-learned potentials. *J. Phys. Chem. C* **2023**, *127*, 13773−13781.

(47) Fan, Z.; et al. GPUMD: A package for constructing accurate machine-learned potentials and performing highly efficient atomistic simulations. *J. Chem. Phys.* **2022**, *157*, 114801.

(48) Fan, Z.; Chen, W.; Vierimaa, V.; Harju, A. Efficient molecular dynamics simulations with many-body potentials on graphics processing units. *Comput. Phys. Commun.* **2017**, *218*, 10−16.

(49) Blöchl, P. E. Projector augmented-wave method. *Phys. Rev. B* **1994**, *50*, 17953.

(50) Kresse, G.; Hafner, J. Ab initio molecular dynamics for liquid metals. *Phys. Rev. B* **1993**, *47*, 558.

(51) Kresse, G.; Furthmüller, J. Efficiency of ab-initio total energy calculations for metals and semiconductors using a plane-wave basis set. *Comput. Mater. Sci.* **1996**, *6*, 15−50.

(52) Sun, J.; Ruzsinszky, A.; Perdew, J. P. Strongly Constrained and Appropriately Normed Semilocal Density Functional. *Phys. Rev. Lett.* **2015**, *115*, 036402.

(53) Lahnsteiner, J.; Kresse, G.; Kumar, A.; Sarma, D. D.; Franchini, C.; Bokdam, M. Room-temperature dynamic correlation between methylammonium molecules in lead-iodine based perovskites: An ab initio molecular dynamics perspective. *Phys. Rev. B* **2016**, *94*, 214114.

(54) Fan, Z.; Zeng, Z.; Zhang, C.; Wang, Y.; Song, K.; Dong, H.; Chen, Y.; Ala-Nissila, T. Neuroevolution machine learning potentials: Combining high accuracy and low cost in atomistic simulations and application to heat transport. *Phys. Rev. B* **2021**, *104*, 104309.

(55) *CALORINE*. https://gitlab.com/materials-modeling/calorine, 2023 (accessed 2023-06-17).

(56) Larsen, A. H.; et al. The atomic simulation environment − a Python library for working with atoms. *J. Phys.: Condens. Matter* **2017**, *29*, 273002.

(57) Wierstra, D.; Schaul, T.; Glasmachers, T.; Sun, Y.; Peters, J.; Schmidhuber, J. Natural Evolution Strategies. *Journal of Machine Learning Research* **2014**, *15*, 949−980.

(58) Berendsen, H. J. C.; Postma, J. P. M.; van Gunsteren, W. F.; DiNola, A.; Haak, J. R. Molecular dynamics with coupling to an external bath. *J. Chem. Phys.* **1984**, *81*, 3684.

(59) Torrie, G.; Valleau, J. Nonphysical sampling distributions in Monte Carlo free-energy estimation: Umbrella sampling. *J. Comput. Phys.* **1977**, *23*, 187−199.

(60) Kumar, S.; Rosenberg, J. M.; Bouzida, D.; Swendsen, R. H.; Kollman, P. A. Multidimensional free-energy calculations using the weighted histogram analysis method. *J. Comput. Chem.* **1995**, *16*, 1339−1350.

(61) Grossfield, A. WHAM: the weighted histogram analysis method, version 2.0.11, 2022, http://membrane.urmc.rochester.edu/wordpress/?page_id/126 (accessed 2023-06-17).

(62) Klarbring, J. Low-energy paths for octahedral tilting in inorganic halide perovskites. *Phys. Rev. B* **2019**, *99*, 104105.

(63) Stukowski, A. Visualization and analysis of atomistic simulation data with OVITO − the Open Visualization Tool. *Modell. Simul. Mater. Sci. Eng.* **2010**, *18*, 015012.

(64) Glazer, A. M. The classification of tilted octahedra in perovskites. *Acta Crystallographica B* **1972**, *28*, 3384−3392.

(65) Sharma, S.; Weiden, N.; Weiss, A. Phase Transitions in $CsSnCl_3$ and $CsPbBr_3$ An NMR and NQR Study. *Zeitschrift für Naturforschung A* **1991**, *46*, 329−336.

(66) López, C. A.; Abia, C.; Alvarez-Galván, M. C.; Hong, B.-K.; Martínez-Huerta, M. V.; Serrano-Sánchez, F.; Carrascoso, F.; Castellanos-Gómez, A.; Fernández-Díaz, M. T.; Alonso, J. A. Crystal Structure Features of $CsPbBr_3$ Perovskite Prepared by Mechano-chemical Synthesis. *ACS Omega* **2020**, *5*, 5931−5938.

(67) Svirskas, Š.; Balčiūnas, S.; Šimėnas, M.; Usevičius, G.; Kinka, M.; Velička, M.; Kubicki, D.; Castillo, M. E.; Karabanov, A.; Shvartsman, V. V.; de Rosário Soares, M.; Šablinskas, V.; Salak, A. N.; Lupascu, D. C.; Banys, J. Phase transitions, screening and dielectric response of $CsPbBr_3$. *Journal of Materials Chemistry A* **2020**, *8*, 14015−14022.

(68) Malyshkin, D.; Sereda, V.; Ivanov, I.; Mazurin, M.; Sednev-Lugovets, A.; Tsvetkov, D.; Zuev, A. New phase transition in $CsPbBr_3$. *Mater. Lett.* **2020**, *278*, 128458.

(69) Quarti, C.; Mosconi, E.; De Angelis, F. Interplay of orientational order and electronic structure in methylammonium

lead iodide: implications for solar cell operation. *Chem. Mater.* **2014**, *26*, 6557−6569.

(70) Maheshwari, S.; Fridriksson, M. B.; Seal, S.; Meyer, J.; Grozema, F. C. The Relation between Rotational Dynamics of the Organic Cation and Phase Transitions in Hybrid Halide Perovskites. *J. Phys. Chem. C* **2019**, *123*, 14652−14661.

(71) Sukmas, W.; Sakulsupich, V.; Tsuppayakorn-aek, P.; Pinsook, U.; Pakornchote, T.; Klinkla, R.; Bovornratanaraks, T. Preferred oriented cation configurations in high pressure phases IV and V of methylammonium lead iodide perovskite. *Sci. Rep.* **2020**, *10*, 21138.

(72) Cordero, F.; Trequattrini, F.; Craciun, F.; Paoletti, A.; Pennesi, G.; Zanotti, G. Cation reorientation and octahedral tilting in the metal-organic perovskites MAPI and FAPI. *J. Alloys Compd.* **2021**, *867*, 158210.

(73) Wu, J.; Chen, J.; Wang, H. Phase Transition Kinetics of MAPbI$_3$ for Tetragonal-to-Orthorhombic Evolution. *JACS Au* **2023**, *3*, 1205−1212.

(74) Mattoni, A.; Filippetti, A.; Saba, M. I.; Delugas, P. Methylammonium Rotational Dynamics in Lead Halide Perovskite by Classical Molecular Dynamics: The Role of Temperature. *J. Phys. Chem. C* **2015**, *119*, 17421−17428.

(75) Chen, T.; Foley, B. J.; Ipek, B.; Tyagi, M.; Copley, J. R. D.; Brown, C. M.; Choi, J. J.; Lee, S.-H. Rotational dynamics of organic cations in the CH$_3$NH$_3$PbI$_3$ perovskite. *Phys. Chem. Chem. Phys.* **2015**, *17*, 31278−31286.

(76) Fabini, D. H.; Siaw, T. A.; Stoumpos, C. C.; Laurita, G.; Olds, D.; Page, K.; Hu, J. G.; Kanatzidis, M. G.; Han, S.; Seshadri, R. *Universal Dynamics of Molecular Reorientation in Hybrid Lead Iodide Perovskites* **2017**, *139*, 16875−16884.